Experimental characterization of scattering from the trihedral corner reflector in the E-band

Allan Wainaina Mbugua,[1] Yun Chen,[2] Simon Tejero Alfageme,[2] Sergio Duque Biarge,[2] and Wei Fan[3,4,✉]

[1]*Huawei Technologies Duesseldorf GmbH, Munich Research Center, Munich, Germany and the Antennas, Propagation and Millimetre-Wave Systems (APMS) Section, Aalborg University, Aalborg, Denmark*

[2]*Huawei Technologies Duesseldorf GmbH, Munich Research Center, Munich, Germany*

[3]*Antennas, Propagation and Millimetre-Wave Systems (APMS) Section, Aalborg University, Aalborg, Denmark*

[4]*Center for Wireless Communication (CWC), Oulu University, Oulu, Finland*

✉ Corresponding author: Wei Fan, Email: wfa@es.aau.dk

Canonical objects with known radar cross section (RCS), for example, the trihedral corner reflector (TCR), play a crucial role in the calibration of automotive radar sensors. Moreover, these canonical objects are also used in the validation of simulated RCS obtained using asymptotic methods, such as hybrid geometric optics (GO) and the physical optics (PO) based methods. However, accurate RCS prediction with asymptotic methods is highly dependent on the individual scattering mechanisms considered in a simulation, for example reflection and diffraction from the TCR surfaces and edges, respectively. Reliable measurements are therefore required to evaluate if a particular interaction mechanism can be neglected to reduce computation complexity without adversely affecting the accuracy of the predicted RCS. In this letter, the monostatic scattering characteristics of three metallic TCRs are investigated with varying geometrical sizes in the E-band, that is, from 60 GHz to 90 GHz. The ultra-wideband (UWB) measurements, which offer a high delay resolution, can enable the identification of the individual scattering mechanisms. Diffraction from the TCR edges is experimentally demonstrated to contribute to a non-negligible scattered power in this frequency band.

Introduction: Automotive radar sensors are essential components in autonomous vehicles due to their ability to detect objects and vulnerable road users even in adverse weather conditions with low visibility [1, 2]. Besides robust design of the radar sensors, consistent quality of the radome and suitable signal processing algorithms, optimal performance of the automotive radar sensors require accurate calibration and extensive testing in typical use case scenarios. Due to the difficulty of performing realistic tests in different conditions and environments, vehicle-in-the-loop (ViL) tests are often employed for this purpose [2–4].

In ViL tests, the objective of using asymptotic methods based on geometric optics (GO), physical optics (PO) or hybrid GO-PO is twofold. First, for the simulation of radar cross section (RCS) signatures of complex and electrically large objects especially in the millimetre-wave (mm-wave) automotive radar band where numerical methods of solving Maxwell's equations would not be feasible due to their overwhelming computation complexity [5]. Second, asymptotic methods are used to estimate and parameterize the scattering centers of complex objects [6, 7]. These scattering centers can then used in virtual scenarios in ViL tests to generate the equivalent RCS signatures instead of using the detailed models of vehicles hence improving the simulation time significantly [7].

The validation of the simulated RCS signatures by asymptotic methods is typically done by evaluating the accuracy of simulated RCS signatures of canonical objects with known RCS signatures such as a sphere, a flat plate or corner reflectors (for example the trihedral corner reflector (TCR)). Spheres are frequently used due to their direction independent RCS in the monostatic case and because the RCS can be easily calculated analytically [8]. However, since the scattered power level from a sphere is low it can be adversely affected by noisy measurements especially at mm-wave frequencies, making it less suitable for such applications. On the other hand, flat plates due to their simple geometry, have a monostatic RCS that can be easily computed but suffer the limitation that the RCS level rapidly decreases as the oblique incidence angle increases [5].

The TCR is thus often preferred due to its high monostatic RCS level even for wide range of incidence angles, making it appropriate for automotive scenarios where wide ranges of incidence angles might occur [9]. Characterization of the TCR via measurements is thus required to ensure that the simulated RCS signatures via asymptotic methods are accurate and realistic. The interaction mechanisms contributing to the RCS signature of a TCR include: single, double, and triple reflections and diffraction from the interior and exterior edges [9]. In microwave frequencies, extensive simulations and measurements have been carried out in the literature to characterize the TCR scattering characteristics, whereby modeling of edge diffracted fields has been shown to improve the RCS simulation accuracy in comparison to measurements [5, 9–12].

Experimental characterization of the TCR in mm-wave frequencies is thus essential for validation of simulated RCS particularly for safety critical applications such as automotive radar in the E-band. The RCS of the TCR has mainly been experimentally characterized in microwave frequencies, for example from 2 GHz to 18 GHz in [13]. Although some works have reported RCS measurements of the TCR in the E-band [2, 14], only the overall RCS is shown hence it is not possible to infer the contribution of each interaction mechanism from the TCR. Furthermore, although diffraction at mm-wave is shown to be non-negligible especially for metallic edges [15], no measurements in the literature to the best of the authors knowledge clearly highlight the contribution of this interaction mechanism for a TCR in the E-band.

To fill this gap in the literature, in this letter, continuous wave ultra-wideband (UWB) measurements in the mm-wave frequency band from 60 GHz to 90 GHz are carried out with a vector network analyzer (VNA) to investigate the contribution of edge diffracted fields to the overall RCS in the monostatic case. This large bandwidth results in a delay resolution of 0.033 ns corresponding to a distance of 1 cm which enables the identification of closely located multipath components. Three metallic TCRs with dimensions 59 mm, 78 mm, and 138 mm and peak RCS values of 5 dBsm, 10 dBsm, and 20 dBsm at 77 GHz, respectively, are analyzed. Diffracted fields from the TCR exterior edges are observed to contribute to the RCS signature, thus highlighting the importance of modeling this interaction mechanism in RCS simulation tools in the E-band.

Theory: The RCS measures how detectable an object is by radar, corresponding to the amount of scattered power back to the source. For an arbitrary object under test (OUT), the RCS σ can be obtained as [16]:

$$\sigma = \lim_{R\to\infty} 4\pi R^2 \frac{|\mathbf{E}_s|^2}{|\mathbf{E}_i|^2}, \tag{1}$$

where $\mathbf{E}_i$ and $\mathbf{E}_s$ are the incidence and scattered fields, respectively, and R is the distance between the OUT and the probe antenna.

The reliable calculation of the RCS hinges upon two main factors. First the scattered fields from the OUT can be reliably separated from the field scattered from other objects in the vicinity of the OUT and second that the incident field on the OUT has a planar wave front [16]. The former condition is easily satisfied using time gating techniques with sufficient measurement bandwidth [17]. In RCS measurements setups, the latter condition is satisfied by using compact range measurements setups [8, 18] or by placing the OUT at a sufficient distance from the probe antenna. The sufficient distance largely depends on the OUT under consideration. For example OUTs whose RCS is represented by independent scatter centers allow for a less strict requirement on the variation of the amplitude and phase of the impinging wave compared to flat surfaces [16]. The minimum distance, $R_{\min}$, required to satisfy a given amplitude and phase of the impinging wave at the OUT can be determined using [16, (11) and (12)].

The RCS can also be calculated using the radar range equation [8]:

$$P_r = \frac{P_t G_t G_r \lambda^2 \sigma K}{(4\pi)^3 R^4}, \tag{2}$$

where P_r, P_t, G_t, G_r, λ, K are the receiver (Rx) power, transmitter (Tx) power, gain of the Tx antenna, gain of the Rx antenna, the wavelength, and the system losses, respectively. However, when any of these

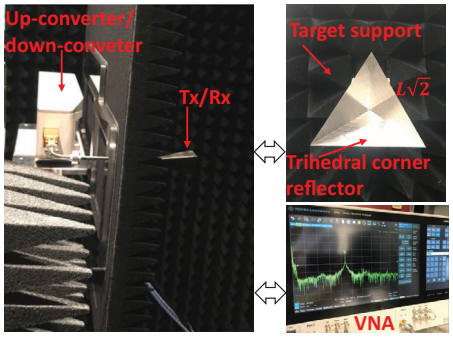

(a)

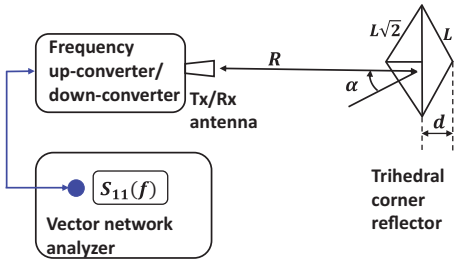

(b)

Fig. 1 *The monostatic measurement setup. (a) Photo of the measurement setup. (b) An illustration of the measurement setup configuration.*

parameters are not known precisely, the calculated RCS would be erroneous. To mitigate this, the RCS of an arbitrary OUT can be calculated accurately by comparing the received power, P_r, to that of a canonical objects whose RCS can be calculated analytically. The peak monostatic RCS σ^{peak} of the TCR occurs when the bottom surface is tilted at an angle $\alpha = \arctan(\frac{1}{\sqrt{2}})$ radians [5, 19].

$$\sigma^{\text{peak}} = \frac{4\pi L^4}{3\lambda^2}, \tag{3}$$

where L is the length of the interior edge of the TCR.

Measurement setup: The measurement is carried out using a VNA and a vertically polarized horn antenna as shown in Figure 1. To minimize the signal loss in the coaxial cables at the considered mm-wave frequency band, the Tx and Rx signals are up-converted and down-converted using a frequency up- and down-converter. The frequency up- and down-converter contains a microwave circulator which enables the use of one antenna for both Tx and Rx and consequently achieving a monostatic RCS measurement setup. The antenna gain of the Tx/Rx increases quasi linearly from 24.5 dBi at 60 GHz to 26.7 dBi at 90 GHz.

Three TCRs are considered with an interior edge length L of 59 mm, 78 mm, and 138 mm whose peak RCS values can be calculated using (3) as 5 dBsm, 10 dBsm, and 20 dBsm, respectively, at 77 GHz. The TCRs are mounted on a metallic stand covered with absorbers as shown in Figure 1. Measurements are then conducted for three cases: (1) with each of the TCRs mounted on the stand, (2) with only the target support, and (3) with the target and TCR removed from the measurement facility. The channel frequency response (CFR) for each of these case is then stored as reflection coefficient S-parameter $S_{11}(f)$.

The minimum distance is determined using [16, (11) and (12)] by considering the largest dimension of the 138 mm TCR at 90 GHz. By fixing the maximum allowable amplitude variation to 1 dB, and relaxing the requirement on the maximum phase variation at the OUT to 78.3 degrees, a measurement distance of $R = 6.55$ is found to be sufficient as illustrated in Figure 2. The suitable distance R is determined from Figure 2b as the region above the intersection of the amplitude and phase curves. Indeed as outlined in [20], the conventional far field condition, that is, setting a requirement of a maximum amplitude and phase variation of 1 dB and 22.5 degrees, respectively, is often too stringent since in this case it would have resulted in a minimum distance of 22.85 m

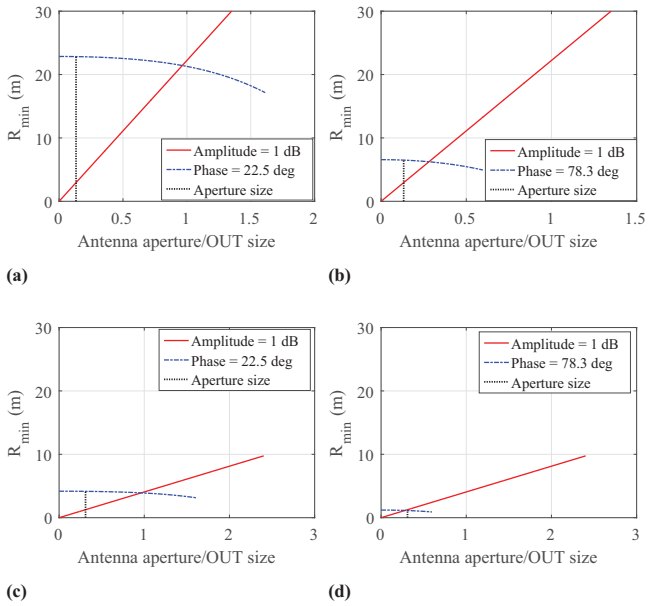

Fig. 2 *An illustration of the minimum distance required for a given maximum allowable amplitude and phase variation at 90 GHz for the TCR cf. [16, (11) and (12)]. (a) Conventional constraints for the 138 mm TCR. (b) Imposed constraints in this work for the 138 mm TCR. (c) Conventional constraints for the 59 mm TCR. (d) Imposed constraints in this work for the 59 mm TCR.*

Table 1. Measurement parameters.

Parameter	Value
Antenna & OUT height	1.3 m
Antenna - OUT distance (R)	6.55 m
Center frequency	75 GHz
VNA intermediate frequency (IF) bandwidth	500 Hz
VNA bandwidth	30 GHz
Number of frequency points	30001
VNA port 1 power	0 dBm

as shown in Figure 2a, leading to high cost and link budget issues. The minimum distance required for the 59 mm TCR at 90 GHz is shown in Figures 2c and 2d for the conventional far field condition and the constraint imposed in this work, respectively, for comparison purposes. The rest of the measurement parameters are outlined in Table 1.

Results and discussion: The measured CFR, that is, $S_{11}(f)$ is multiplied with a Kaiser window with $\beta = 6$ and then transformed to the time domain using the inverse Fourier transform. The three TCRs are each characterized by two distinct contributions in the delay bins from 43 ns to 44 ns as illustrated in Figure 3. An appropriate window, for example, the Kaiser window used here in is thus critical for this application since spectral leakage from the dominant path would mask the closely located weaker path [21]. The dominant peak, path 2, in each case is located at the delay bin 43.7 ns which corresponds to the triply reflected field. Path 1 for the 59 mm, 78 mm, and 138 mm TCRs is located at the delay bins 43.47 ns, 43.4 ns, and 43.17 ns, respectively. This contribution can be demonstrated to originate from the TCR exterior edges as follows. Let d be the distance between the TCR origin and the exterior edges as illustrated in Figure 1. In the monostatic case for the normal incidence, d can be calculated as:

$$d = \sqrt{L^2 - \left(\frac{L\sqrt{2}}{2}\right)^2} \cdot \cos(\alpha). \tag{4}$$

When we have $\alpha = \arctan(\frac{1}{\sqrt{2}})$, the calculated and measured distance between the TCR origin and the exterior edges is outlined in Table 2.

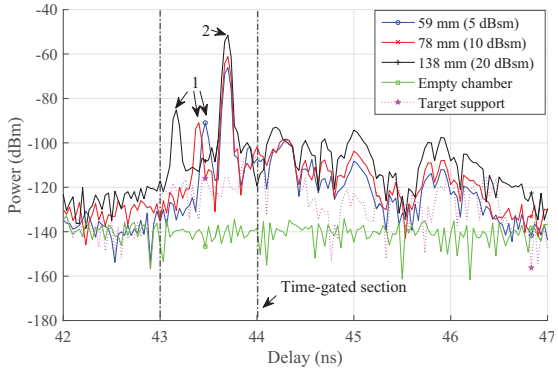

Fig. 3 *The CIR of the three TCR, target support and empty chamber before coherent background subtraction. A Kaiser window with $\beta = 6$ is used in the frequency domain before the inverse Fourier transform.*

Table 2. Calculated and measured parameter of the TCRs.

TCR	Calculated d	Measured d	Path 1 gain	Path 2 gain
59 mm	34.1 mm	34.5 mm	−90.9 dBi	−66 dBi
78 mm	45 mm	45 mm	−90.9 dBi	−61.1 dBi
138 mm	79.7 mm	79.5 mm	−85 dBi	−51.5 dBi

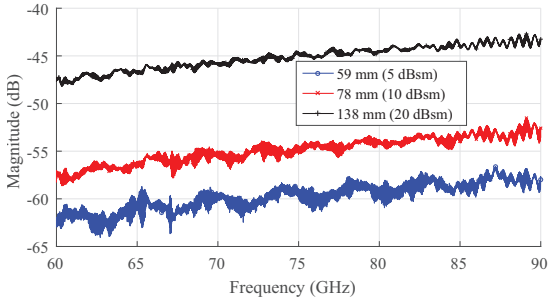

Fig. 4 *The measured CFR of the TCRs with coherent background subtraction and no time-gating.*

For each of the TCRs, path 1 in the channel impulse response (CIR) (i.e. the Fourier transform pair of the CFR in the time domain) illustrated in Figure 3 can thus be concluded to be as a result of diffraction from the exterior edges of the TCRs.

Scattering from the measurement facility walls can be observed to be absent where the OUT is located. Furthermore, although the target support is covered by absorbers some power is scattered back to the Rx antenna. Nonetheless, the scattered power level from target support is below 20 dB in comparison to the weakest diffraction contributions (path 1) from the three TCRs as shown in Figure 3. The comparison of the magnitude difference between the triply reflected path and the edge diffracted paths is outlined in Table 2 for the normal incidence angle. Note that at the off-normal incidence angles, the contribution of triply reflected paths gradually diminishes in magnitude thus the relative contribution of diffracted fields to the overall RCS increases [5, 9–12]. These important observations in the literature and the measurement results shown here demonstrate that diffraction in the E-band is still relevant for accurate RCS calculation especially at off-normal incidence angles.

The measured CFR, that is, $S_{11}(f)$ is dominated by the antenna coupling contribution. Coherent background subtraction is thus performed to minimize this contribution as well as other contributions from the walls of the measurement facility [17, 20]. This results in the CFR illustrated in Figure 4. Due to possible interaction between the TCRs and the target support as can be observed in the delay bins from 44 ns to 47 ns in Figure 3, ripples can still be observed in the CFR. Additionally, the TCRs contribute to delayed reflections which cannot be eliminated by coherent background subtraction. A Tukey window with $\beta = 0.5$ [21] is applied in the delay bins from 43 ns to 44 ns to isolate the contribution of the TCRs. The time-gated CIR is then converted to the frequency domain using the Fourier transform. This results in the CFR shown in

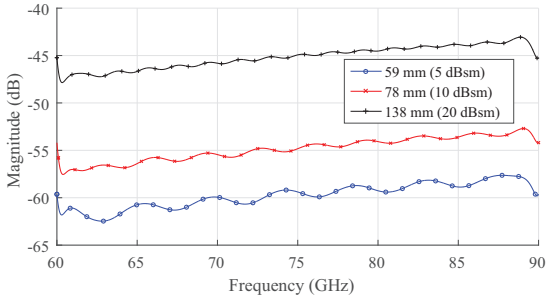

Fig. 5 *The measured CFR of the TCRs after time-gating. Edge effects due to the time-gate thus limit the usable frequency to the range between 63 GHz and 87 GHz.*

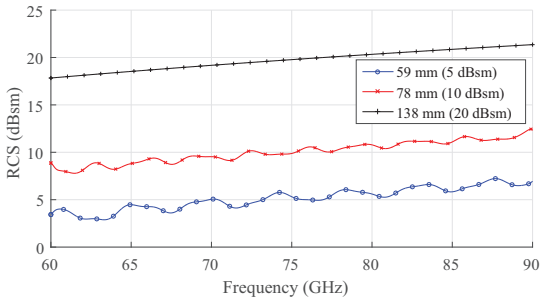

Fig. 6 *The measured monostatic RCS of the TCRs. The 138 mm TCR is selected as the reference OUT hence its flat RCS pattern across frequency.*

Figure 5 containing the contribution of only path 1 and path 2. This is in contrast to the CFR in Figure 4 which contains contributions from the target support and delayed reflections from the TCRs. Note that the CFR resulting from the time-gating operation is then divided using the Kaiser window initially applied during the transformation from the frequency to the time domain.

Time-gating or range-gating used in the isolation of the target scattering causes errors at the edge frequencies in the resulting CFR [18, 22]. Due to the edge effects that occurs as a result of the time-gate applied, the useful frequency range for RCS analysis is selected from 63 GHz to 87 GHz as shown in Figure 5.

The RCS across frequency of the OUT σ^{OUT} can then be calculated as [20]:

$$\sigma^{\mathrm{OUT}} = S_{11}^{\mathrm{OUT}}(f) - (S_{11}^{\mathrm{ref}}(f) - \sigma_{\mathrm{ref}}^{\mathrm{peak}}), \tag{5}$$

where $S_{11}^{\mathrm{OUT}}(f)$ and $S_{11}^{\mathrm{ref}}(f)$ are the magnitude of the time-gated CFR of the OUT and the reference OUT in decibels, respectively, and $\sigma_{\mathrm{ref}}^{\mathrm{peak}}$ is the peak RCS of the reference OUT in decibels obtained using (3). The resulting RCS is shown in Figure 6 where the 138 mm TCR is selected as the reference OUT hence its flat RCS pattern across frequency.

The accuracy of the measured RCS can be clearly observed in Figure 6. The relative RCS difference across frequency between the reference TCR (138 mm) and the 78 mm and 59 mm TCR can observed to be 10 dBsm and 15 dBsm, respectively, which agrees well with the analytic calculation using (3).

Conclusion: In this letter, the measured monostatic RCS of three TCRs is considered with an interior edge length L of 59 mm, 78 mm, and 138 mm in the frequency range from 60 GHz to 90 GHz. Although the monostatic RCS in the boresight direction is dominated by triply reflected fields, weaker diffracted fields from the TCRs exterior edges are observed to be non-negligible and indeed cause the RCS across frequency to exhibit a constructive and destructive pattern. This is more evident in the smallest TCR as the relative difference between the triply reflected and edge diffracted fields becomes smaller with the reduction in the TCR effective area [9]. Similar to the case at microwave frequencies, the measured RCS highlights the importance of modeling diffraction when simulating the RCS of the TCR using asymptotic methods in the mm-wave frequency band.

Author contributions: Allan Wainaina Mbugua: Conceptualization; Data Curation; Formal Analysis; Funding Acquisition; Investigation; Methodology; Project Administration; Resources; Software; Supervision; Validation; Visualization; Writing – Original – Draft; Writing – Review – Editing; Yun Chen: Methodology; Project Administration; Supervision; Writing – Original – Draft; Writing – Review – Editing; Simon Tejero Alfageme: Investigation; Methodology; Validation; Writing – Original – Draft; Writing – Review – Editing; Sergio Duque Biarge: Methodology; Resources; Writing – Original – Draft; Writing – Review – Editing; Wei Fan: Conceptualization; Funding Acquisition; Methodology; Project Administration; Supervision; Writing – Original – Draft; Writing – Review – Editing.

Acknowledgements: This work was supported by Huawei Technologies Duesseldorf GmbH.

Conflict of interest statement: The authors have declared no conflict of interest.

Data availability statement: Research data are not shared.

Received: *18 January 2023* Accepted: *13 April 2023*
doi: 10.1049/ell2.12804

References

1 Bilik, I., Longman, O., Villeval, S., Tabrikian, J.: The rise of radar for autonomous vehicles: signal processing solutions and future research directions. *IEEE Signal Process. Mag.* **36**(5), 20–31 (2019)
2 Abadpour, S., Marahrens, S., Pauli, M., Siska, J., Pohl, N., Zwick, T.: Backscattering behavior of vulnerable road users based on high-resolution RCS measurements. *IEEE Trans. Microw. Theory Techn.* **70**(3), 1582–1593 (2022)
3 Holder, M., Rosenberger, P., Winner, H., D'hondt, T., Makkapati, V.P., Maier, M., Schreiber, H., Magosi, Z., Slavik, Z., Bringmann, O., Rosenstiel, W.: Measurements revealing challenges in radar sensor modeling for virtual validation of autonomous driving. in Proc. 21st Int. Conf. Intell. Transp. Syst., pp. 2616–2622. (2018)
4 Diewald, A., Kurz, C., Kannan, P.V., Gießler, M., Pauli, M., Göttel, B., Kayser, T., Gauterin, F., Zwick, T.: Radar target simulation for vehicle-in-the-loop testing. *Vehicles* **3**(2), 257–271 (2021) [Online]. Available: https://www.mdpi.com/2624-8921/3/2/16
5 Weinmann, F.: Ray tracing with PO/PTD for RCS modeling of large complex objects. *IEEE Trans. Antennas Propag.* **54**(6), 1797–1806 (2006)
6 Schuler, K., Becker, D., Wiesbeck, W.: Extraction of virtual scattering centers of vehicles by ray-tracing simulations. *IEEE Trans. Antennas Propag.* **56**(11), 3543–3551 (2008)
7 Buddendick, H., Eibert, T.F.: Incoherent scattering-center representations and parameterizations for automobiles [EM Programmer's Notebook]. *IEEE Antennas Propag. Mag.* **54**(1), 140–148 (2012)
8 Dybdal, R.: Radar cross section measurements. *Proc. IEEE* **75**(4), 498–516 (1987)
9 Polycarpou, A.C., Balanis, C.A., Birtcher, C.R.: Radar cross section of trihedral corner reflectors using PO and MEC. *Ann. Des Télécommun.* **50**(5), 510–516 (1995)
10 Baldauf, J., Lee, S.-W., Lin, L., Jeng, S.-K., Scarborough, S., Yu, C.: High frequency scattering from trihedral corner reflectors and other benchmark targets: SBR versus experiment. *IEEE Trans. Antennas Propag.* **39**(9), 1345–1351 (1991)
11 Shah, M.A., Tokgöz, C., Salau, B.A.: Radar cross section prediction using iterative physical optics with physical theory of diffraction. *IEEE Trans. Antennas Propag.* **70**(6), 4683–4690 (2022)
12 He, Y., He, H., Hu, C., Yin, J., Yang, J.: Polarization analysis of trihedral corner reflector with high-frequency approximation. *IEEE Trans. Antennas Propag.* **70**(10), 9607–9620 (2022)
13 Kashyap, S., Stanier, J., Louie, A., Mishra, S., Larose, C.: RCS of a trihedral corner reflector. In: International Symposium on Antenna Technology and Applied Electromagnetics (ANTEM), pp. 158–163. IEEE, Piscataway (1994)
14 Buchberger, C., Eder, T., Pfeiffer, F., Biebl, E.: Analytical model for the maximum radar cross section of dielectric trihedral corner reflectors. In: Proceedings of IEEE Radar Conference, pp. 1–5. IEEE, Piscataway (2022)
15 Jacob, M., Priebe, S., Dickhoff, R., Kleine-Ostmann, T., Schrader, T., Kurner, T.: Diffraction in mm and sub-mm wave indoor propagation channels. *IEEE Trans. Microw. Theory Techn.* **60**(3), 833–844 (2012)
16 Kouyoumjian, R., Peters, L.: Range requirements in radar cross-section measurements. *Proc. IEEE* **53**(8), 920–928 (1965)
17 IEEE recommended practice for radar cross-section test procedures. IEEE Std 1502-2020 (Revision of IEEE Std 1502-2007), pp. 1–78. IEEE, Piscataway (2020)
18 Ezuma, M., Anjinappa, C.K., Funderburk, M., Guvenc, I.: Radar cross section based statistical recognition of UAVs at microwave frequencies. *IEEE Trans. Aerosp. Electron. Syst.* **58**(1), 27–46 (2022)
19 Sarabandi, K., Chiu, T.-C.: Optimum corner reflectors for calibration of imaging radars. *IEEE Trans. Antennas Propag.* **44**(10), 1348–1361 (1996)
20 Jarvis, R.E., Metcalf, J.G., Ruyle, J.E., McDaniel, J.W.: Wideband measurement techniques for extracting accurate RCS of single and distributed targets. *IEEE Trans. Instrum. Meas.* **71**, 1–12 (2022)
21 Harris, F.: On the use of windows for harmonic analysis with the discrete fourier transform. *Proc. IEEE* **66**(1), 51–83 (1978)
22 Chen, Z., Xiong, Z.: Mitigation of band edge effects in fourier transform based time domain gating. In: European Conference on Antennas and Propagation (EUCAP), pp. 1–5. IEEE, Piscataway (2019)